Journal of Materials Chemistry C

ROYAL SOCIETY OF CHEMISTRY

PAPER

View Article Online
View Journal | View Issue

Cite this: J. Mater. Chem. C, 2025, 13, 5700

Development of a PVDF/1D–2D nanofiller porous structure pressure sensor using near-field electrospinning for human motion and vibration sensing†

Ravinder Reddy Kisannagar, [a] Jaehyuk Lee,[a] Yoonseok Park [b] and Inhwa Jung *[a]

Received 13th December 2024,
Accepted 21st January 2025

DOI: 10.1039/d4tc05253f

rsc.li/materials-c

Flexible pressure sensors with multifunctional capabilities are crucial for a wide range of applications, including health monitoring, human motion detection, soft robotics, tactile sensing, and machine vibration monitoring. In this study, we investigate the development and characterization of a high-performance pressure sensor fabricated using near-field electrospinning (NFES) of 1D–2D nanofiller (NF) incorporated polyvinylidene fluoride (PVDF) hybrid nanocomposite (PVDF/NF) ink. NFES is considered a highly effective and advanced printing technology, capable of producing 3D porous structures with intricate complexity, offering precise control over their material properties and morphology. The sensor's performance is thoroughly evaluated based on key parameters, including a pressure range of 0–300 kPa, sensitivity between 0.014 and 10.67 kPa^{-1}, a rapid response time of 16 ms, a minimal hysteresis of 9.62%, exceptional durability over 1500 cycles, and the ability to detect pressure frequencies up to 500 Hz. These results highlight the PVDF/NF sensor's versatility and demonstrate its potential for a wide range of applications, from low-frequency pressure variations associated with human motion to high-frequency pressure fluctuations typical of machine vibrations. Future studies could focus on selecting and optimizing the material composition for the fabrication of porous structure sensors *via* NFES, aiming to enhance both sensor performance and its multi-functionality in practical applications.

1. Introduction

Flexible pressure sensors play a vital role in a variety of applications, ranging from health monitoring and human motion detection to posture recognition, soft robotics, tactile sensing, and machine vibration sensing, among others.[1–6] Pressure sensors are categorized into four types: piezo-resistive, capacitive, piezoelectric, and triboelectric sensors.[7–12] Among these, piezo-resistive pressure sensors, which respond to mechanical pressure by varying electrical resistance or current, are simple, cost-effective, and adaptable to a broad range of materials and manufacturing processes. Moreover, they operate with minimal power consumption, making them highly energy-efficient and offer easy signal detection. Piezo-resistive pressure sensors employ various conductive materials as sensing elements, including metal nanoparticles/wires, carbon-based materials, conductive polymers, MXenes, and soft platform materials such as polymers, textiles, and papers.[13,14] The demand for multi-functional sensors is rapidly increasing, with the ability to detect various mechanical stimuli, including pressure and vibration, to address the diverse needs of advanced applications in healthcare, robotics, and industrial diagnostics. To date, various designs, materials, and methods have been reported to enhance sensor performance including sensing range, sensitivity, response time, *etc.*, though many offer limited functionality.[13,15]

For instance, Wei *et al.* developed a piezoresistive pressure sensor by embedding graphene/single-walled carbon nanotubes (SWCNTs) into paper as the active layer, featuring a double zig-zag design and silver interconnects as electrodes, which showed improved performance.[16] The developed sensor exhibited a sensitivity of 12.07 kPa^{-1}, a maximum pressure sensing range of 60 kPa, and a response time of 330 ms. Wang *et al.* fabricated a sensor by coating air-laid cellulose with PEDOT:PSS and employing a Cu-interdigitated electrode design, resulting in a sensor with exceptional sensitivity ranging from 93 to 768.07 kPa^{-1}, a pressure range of up to 250 kPa, and a response time of 120 ms.[17] Moreover, the performance of the piezoresistive pressure sensor

[a] Department of Mechanical Engineering, Kyung Hee University, Yongin, 17104, Korea. E-mail: ijung@khu.ac.kr
[b] Department of Advanced Materials Engineering for Information & Electronics, Kyung Hee University, Yongin, 17104, Korea

† Electronic supplementary information (ESI) available. See DOI: https://doi.org/10.1039/d4tc05253f

is enhanced by placing a spacer with a crosshair grid design between the active layer and the electrode or by employing a rough electrode.[18,19] However, the dynamic response of the sensor has not been studied in these reports.

Among the various methods, electrospinning (both far-field and near-field) offers a facile, cost-effective, and scalable way to produce porous structures with controllable morphology, which is essential for the fabrication of high-performance flexible devices suitable for a wide range of applications.[20–23] For example, Zhang *et al.* developed a piezoresistive pressure sensor by electrospinning an ionic liquid (IL) IL/MWCNT/PVDF composite.[24] The developed sensor exhibited a sensitivity of 0.075 kPa^{-1}, a pressure sensing range of up to 307 kPa, and a response time of 120 ms. Zhou *et al.* fabricated a sensor by dip-coating electrospun PVDF fibers with a polyvinyl alcohol-carbon nanotube (PVA-CNT) solution mixture, resulting in a sensor with a sensitivity of 0.0196 kPa^{-1} within a pressure range of up to 40 kPa and a hysteresis of 13.1%.[25] Simon *et al.* developed a sensor by electrospinning PVDF containing graphene nanoplatelets (GNP) functionalized with ILs.[26] The sensor demonstrated a sensitivity of approximately 0.6 kPa^{-1}, which decreases with increasing applied strain rate, and exhibited low hysteresis within the working range of 0 to 250 kPa. Most pressure sensors fabricated by the electrospinning method exhibit low sensitivity and slow response times.[24,25,27–32] One approach involves preparing a polymer fibrous network through electrospinning, followed by coating it with conductive materials, while another approach uses electrospinning of conductive polymer composites.[24,25] Traditional electrospinning often results in fibers with low mechanical strength or irregular morphology. Additionally, large compression deformation at slightly lower pressures and poor electrical responses, possibly due to insufficient contact between fibers under pressure, may lead to low sensitivity, a limited pressure range, and slow response times.[23] Sensors with high sensitivity with a broad pressure range, negligible hysteresis and fast response times are needed for static and dynamic pressure sensing, with applications in wearable and vibration sensing. The low-pressure range (0–10 kPa) detects subtle pressures like pulse and soft touch, the medium range (10–100 kPa) monitors human motion and health, and the high-pressure range is suited for industrial applications.[33,34]

In this work, we developed a pressure sensor employing PVDF/NF ink using NFES. NFES is recognized as a sophisticated and efficient printing technology, capable of fabricating 3D porous structures with complex geometries due to the low applied voltage and working distance while providing precise control over material properties and morphology.[22,23] The incorporation of 1D–2D nanofillers, such as multi-walled carbon nanotubes (MWCNTs), reduced graphene oxide (rGO), and silver nanowires (AgNWs), into the PVDF matrix facilitates the percolation threshold, improving electrical conductivity and mechanical strength while maintaining flexibility and scalability, making it a promising material for advanced pressure sensing applications. The PVDF/NF sensor exhibited a pressure range of 0–300 kPa, sensitivity between 0.014 and 10.67 kPa^{-1}, a quick response time of 16 ms, minimal hysteresis of 9.62%, outstanding durability over 1500 cycles, and the capability to detect pressure frequencies as high as 500 Hz. Furthermore, we demonstrated the sensor's applications in detecting human motion such as finger and wrist-knee bending, wrist pulse for vital sign monitoring as well as sensing vacuum pump vibrations and compared it with that of a commercial accelerometer.

2. Experimental section

2.1 Materials

PVDF powder (M_w ~ 534 000) was procured from Sigma-Aldrich. MWCNT-COOH (carboxyl-functionalized, outer diameter ~10–20 nm, length ~10–30 μm, purity > 95%) was purchased from Cheaptubes, USA. rGO (specific surface area ~600–900 $m^2 g^{-1}$, thickness ~2.0–2.4 nm) was obtained from (rGO-V20, Standard Graphene, Korea). AgNW solution (1 wt% AgNWs in IPA, diameter ~20–40 nm, length ~10–20 μm, DT-AGNW-N30-1IPA) was procured from Ditto Technology, Korea. Acetone (99.5%) and dimethylformamide (DMF) (99.5%) were purchased from Samchun Chemicals, South Korea. Carbon (1 μm thick) coated Al foil (double side, 15 μm thick) was procured from Welcos, Korea. PET (thickness 100 μm) was obtained from commercial sources.

2.2 Ink preparation

The process diagram for ink preparation is shown in Fig. 1(a). To prepare the 1D–2D nanofiller dispersed polyvinylidene fluoride hybrid nanocomposite ink (PVDF/NF), 12 mg of rGO and 6 mg of MWCNT-COOH were initially added to a glass vial containing 2 mL of acetone and 2 mL of DMF. The solution was then subjected to simultaneous ultra-sonication (VC-505, Sonics, USA) and magnetic stirring at 300 rpm while maintaining the temperature at 95 °C for 1 h to achieve well-dispersed nanomaterials. Subsequently, 1.2 g of PVDF powder was added to the vial, followed by the addition of 1.5 mL of AgNW solution and 4.5 mL of acetone. The mixture was then stirred at 200 rpm and heated at 95 °C until small bubbles began to form, indicating the dissolution of PVDF (approximately 3 min). Finally, the resulting PVDF/NF ink was allowed to cool to room temperature for further use.

2.3 Printing of the PVDF/NF-based porous structure by NFES

The PVDF/NF active layer for the pressure sensor was fabricated *via* NFES under ambient conditions. The typical setup for printing is shown in Fig. 1(b). The setup consisted of a syringe pump (Legato 100, KD Scientific, USA), a DC power supply system (High Voltage Supplier 30 kV, IDKLAB, Korea), and 3-axis motion stages. The 3-axis motion stages consist of X–Y and Z stages controlled by a self-built LabVIEW program. The prepared PVDF/NF ink was filled into a 5 mL syringe and secured onto the syringe pump, which was then connected to a metal needle (inner diameter ~520 μm, length ~12.7 mm) fixed on the Z-stage *via* a polytetrafluoroethylene (PTFE) tube (inner diameter ~1.59 mm, outer diameter ~3.18 mm). The carbon-coated aluminum foil was mounted on the X–Y movable stage as the collector.

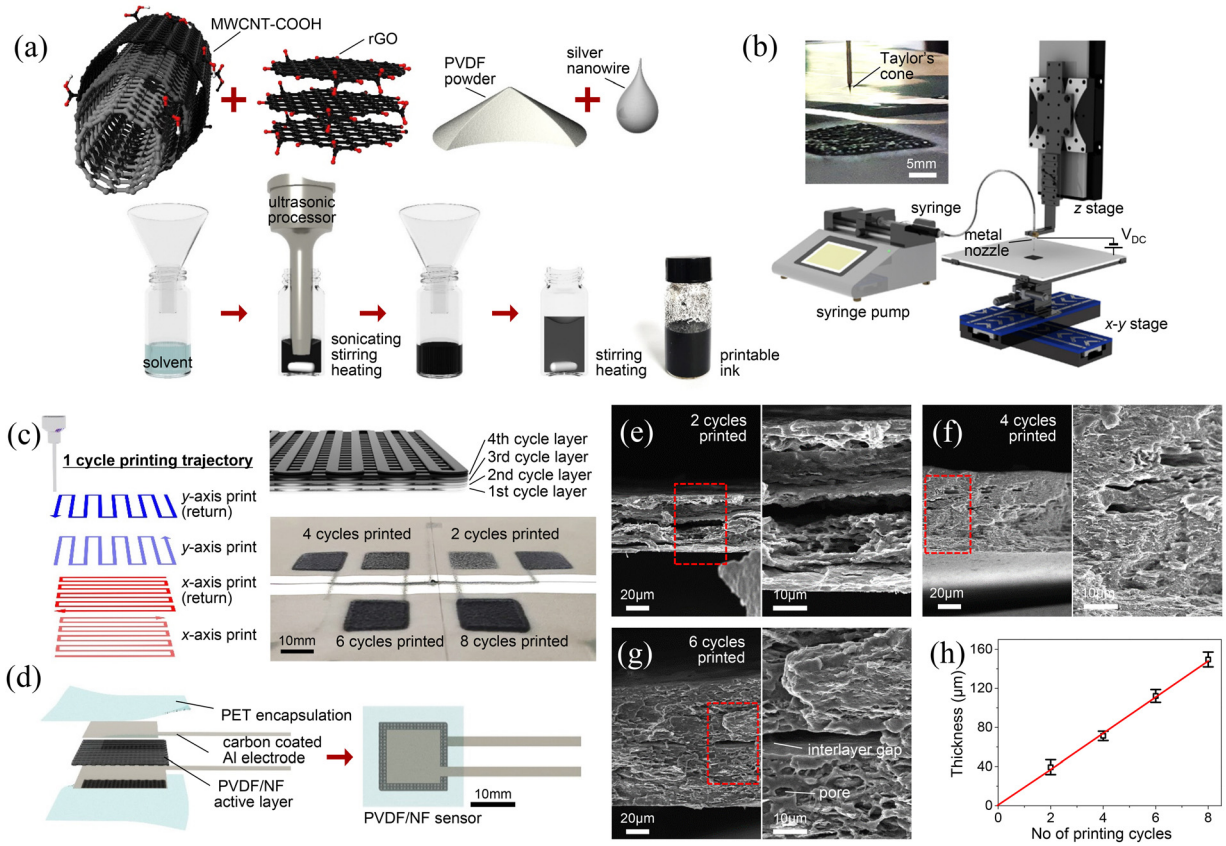

Fig. 1 Ink preparation and device fabrication procedure: (a) schematic of the PVDF/NF ink preparation method, (b) setup for printing PVDF/NF ink using the near-field electrospinning technique, (c) one-cycle printing trajectory (left), schematic of the structure after four printing cycles (upper right), and photos of printed structures with 2, 4, 6, and 8 cycles (lower right), (d) schematic of the sensor fabrication process, (e)–(g) cross-sectional SEM images of PVDF/NF-2, PVDF/NF-4, and PVDF/NF-6, respectively, and (h) thickness of the printed structure as a function of the number of printing cycles.

The process parameters were as follows: the ink flow rate was 0.1 mL min^{-1}, the applied voltage was 3 kV, the X–Y stage velocity was 25 mm s^{-1}, and the distance between the needle and the collector was 10 mm. One printing cycle (18 × 18 mm^2) corresponded to a rectangular trajectory with a width of 1 mm and a length of 18 mm, traversing along both the *X* and *Y* axes. The printing trajectory for one cycle is shown on the left side of Fig. 1(c), while a schematic of the structure after four printing cycles is shown on the top right side of Fig. 1(c). PVDF/NF active layers with 2, 4, 6, and 8 printing cycles were prepared to investigate the effect of the number of printed layers on the device performance. These layers are labeled PVDF/NF-2, PVDF/NF-4, PVDF/NF-6, and PVDF/NF-8, respectively. At the bottom right of Fig. 1(c), photos of the printed structures are provided.

2.4 PVDF/NF sensor fabrication

The PVDF/NF sensor fabrication process is illustrated in Fig. 1(d). A carbon-coated aluminum foil was cut into 12 × 12 mm^2 pieces, with 37 × 3.5 mm^2 rectangular extensions for external connections. The printed PVDF/NF active layer was then sandwiched between the top and bottom electrodes and encapsulated with two layers of adhesive PET. The entire structure was roll-pressed using a hot roller (NW 320M, Nakwon, Korea). To ensure proper sensor connection and minimize electrode damage during operation, a custom connector was designed. A photo of the fabricated sensor with the connector is shown in the ESI,† Fig. S1. The connector was made from polylactic acid (PLA) material using a commercial 3D printer (Ultimaker S3, Ultimaker, Netherlands).

2.5 Structural and electromechanical characterization

The X-ray diffraction patterns of PVDF and PVDF/NF were obtained using an XRD instrument (D8 Advance, Bruker). The surface and cross-sectional morphologies of the PVDF/NF ink and printed layers were analyzed using a field-emission scanning electron microscope (FE-SEM) (Gemini360, Carl Zeiss). High-resolution images of the PVDF/NF ink were captured with a transmission electron microscope (TEM) (JEM-2100F, JEOL). Fourier-transform infrared spectroscopy (FT-IR) of PVDF and PVDF/NF was performed using an FT-IR spectrometer (Spectrum One System, PerkinElmer). Raman spectra of PVDF and PVDF/NF were recorded using a Raman spectrometer (inVia Raman microscope, Renishaw, UK). Electromechanical measurements of the sensor were conducted with a custom-designed material testing system, which includes a single motion stage, a 10 kgf load cell (CDFS-10, BONGSHIN, Korea), a data acquisition system (DAQ) (4ch SCADAS mobile, LMS), and a digital multimeter

(DMM 7510, Keithley). Cyclic pressures at different frequencies were applied using a mini-shaker (2007E, Modal Shop). The cyclic force was measured using a force transducer (208C01, PCB Electronics), and the pressure frequency was controlled by the source generator (4ch SCADAS mobile, LMS). Resistance changes were recorded at a rate of 0.714k samples per s using a digital multimeter and high frequency measurements were recorded at a rate of 5.12k samples per s. Informed consent was obtained for the experiments involving human participants.

3. Results and discussion

Fig. 1(a) shows a schematic illustration of the PVDF/NF ink preparation. In brief, 12 mg of rGO and 6 mg of MWCNT-COOH were added to 2 mL of acetone and 2 mL of DMF, and the mixture was ultrasonicated and stirred at 300 rpm and 95 °C for 1 h. Next, 1.2 g of PVDF powder, 1.5 mL of AgNW solution, and 4.5 mL of acetone were added. The mixture was then stirred at 200 rpm and heated to 95 °C until the PVDF dissolved (approximately 3 min). The ink was cooled and stored for later use. Fig. 1(b) and (c) show the setup for PVDF/NF active layer printing and the printing trajectory for the active layer, and the printed structures for 2, 4, 6, and 8 layers, respectively, whereas Fig. 1(d) shows the device fabrication schematic, as detailed in the experimental section. The extruded PVDF/NF ink meniscus from the spinneret forms a Taylor cone due to the electrostatic field applied between the metal needle and the collector.[21,35] The continuous PVDF/NF jet, induced from the tip of the Taylor cone, is then deposited onto carbon-coated Al foil affixed to a movable X–Y stage, (upper left image) as shown in Fig. 1(b). Fig. 1(e)–(g) show the cross-sectional SEM images of PVDF/NF-2, PVDF/NF-4, and PVDF/NF-6, respectively. The cross-sectional SEM images of PVDF/NF-8 are provided in the ESI,† Fig. S2. As observed in Fig. 1(e)–(g) and Fig. S2 (ESI†), both the thickness of the PVDF/NF active layers and their structural compactness increase with the number of printing cycles, while porosity decreases, as shown in Fig. 1(h). This trend may be attributed to the gradual impregnation of the ink into the voids and porous regions of the underlying layers during the deposition of subsequent layers.

Following the preparation of the ink, it was left to dry at room temperature before further characterization. The SEM images of PVDF/NF at magnifications of ×10k, ×50k, and ×100k are presented in Fig. 2(a)–(c), respectively. The ×50k image is an enlarged view of the red dotted box area in the ×10k image, and similarly, the ×100k image is an enlargement of the red dotted box area in the ×50k image. As observed in these images, the ink displays a porous structure with uniform distribution of rGO, MWCNTs, and AgNWs, randomly interconnected within the PVDF polymer matrix.

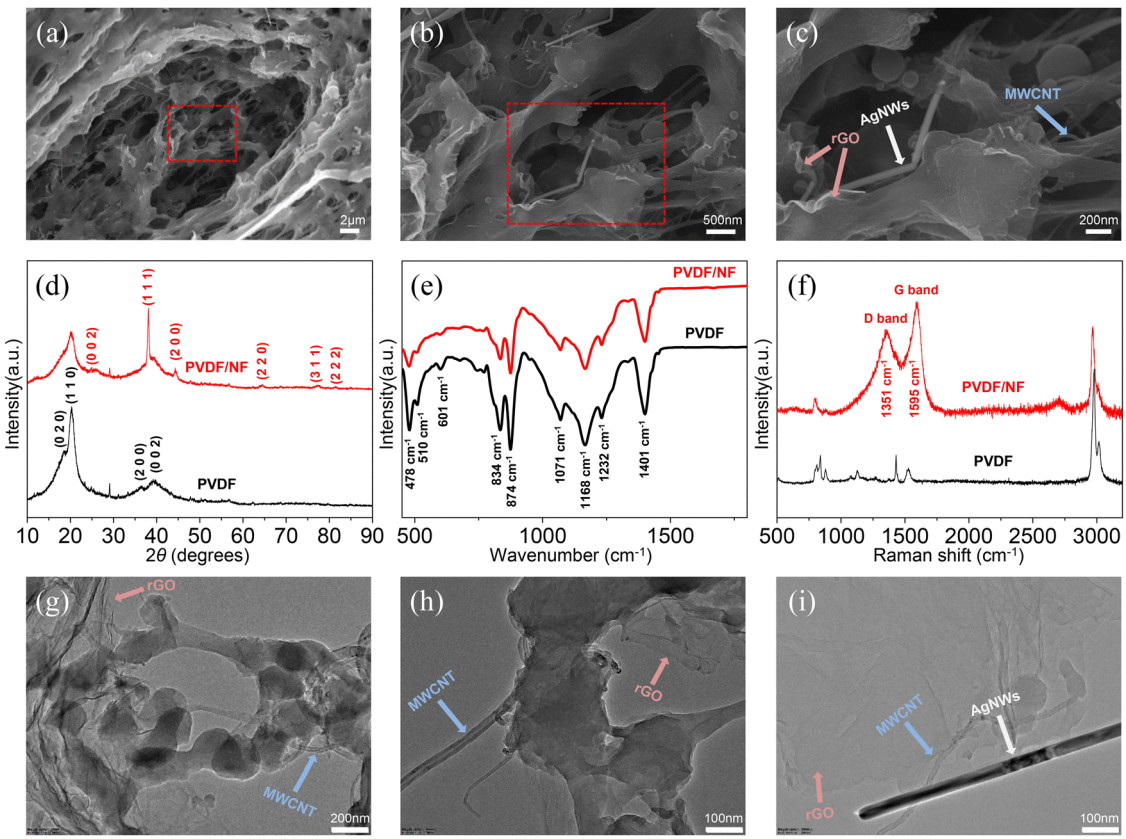

Fig. 2 Characterization of the PVDF/NF ink: (a)–(c) SEM images of PVDF/NF at magnifications of ×10k, ×50k, and ×100k, respectively, (d) XRD patterns comparing PVDF and PVDF/NF, (e) FTIR spectra of PVDF and PVDF/NF, (f) Raman spectroscopy data for PVDF and PVDF/NF, and (g)–(i) TEM images of PVDF/NF.

This arrangement forms a conductive network crucial for the material's piezo-resistive properties, as highlighted in the high-magnification SEM image of Fig. 2(c). The EDS spectra and elemental mapping of PVDF/NF, shown in Fig. S3 (ESI†), confirm the presence of carbon (C), fluorine (F), oxygen (O), and silver (Ag), with their respective atomic weight% (C-72.52%, F-24.84%, Ag-1.22%, and O-1.32%) provided in Table S1 of the ESI.†

Fig. 2(d) presents the XRD patterns of PVDF and PVDF/NF. As shown in the figure, PVDF exhibits diffraction peaks at 2θ values of 18.4°, 20.2°, 36.4°, and 39.5°, which are indexed to the (0 2 0), (1 1 0), (2 0 0), and (0 0 2) planes, respectively.[36,37] In addition to the peaks from PVDF, the XRD pattern of PVDF/NF shows a diffraction peak at 26.01°, corresponding to the (0 0 2) plane, which is attributed to rGO/MWCNTs.[38] Furthermore, additional peaks at 2θ angles of 38.13°, 44.34°, 64.43°, 77.47°, and 81.42° are observed, corresponding to the (1 1 1), (2 0 0), (2 2 0), (3 1 1), and (2 2 2) planes of AgNWs, respectively.[39] Fig. 2(e) shows the FTIR spectra of PVDF and PVDF/NF. The FTIR spectrum of PVDF exhibits characteristic absorption bands at 478, 510, 601, 834, 874, 1071, 1168, 1232, and 1401 cm^{-1}, which correspond to the crystalline phases of α, β, and γ, consistent with values reported in the literature for PVDF.[36,40] The absorption peaks for the α-phase are around 488, 601, and 1071 cm^{-1}, assigned to CF_2 bending and wagging, CF_2 bending and skeletal bending, and CH_2 wagging, respectively.[36,41,42] The characteristic absorption peaks for the β-phase, around 510, 874, 1168, and 1400 cm^{-1}, are assigned to CF bending, C–C–C asymmetrical stretching, CF symmetrical stretching, and CH_2 wagging, respectively.[36,41,42] The peaks at 834 and 1232 cm^{-1} belong to the γ-phase and are attributed to CF stretching and out-of-plane deformation, respectively.[36,41,42] The FTIR spectrum of PVDF/NF shows no significant changes in these absorption bands, suggesting that the nanofillers are encapsulated within the PVDF matrix and that there is no significant chemical interaction between PVDF and the nanofillers.

The Raman spectra of PVDF/NF reveal additional characteristic peaks compared to those of pure PVDF, as shown in Fig. 2(f).[43] Specifically, two distinct peaks at 1351 cm^{-1} and 1595 cm^{-1} are observed, corresponding to the D-band and G-band, respectively, attributed to the vibrational modes of rGO/MWCNTs.[44] Fig. 2(g)–(i) presents high-magnification TEM images of PVDF/NF, revealing the presence of AgNWs, MWCNTs, and rGO sheets, as well as their uniform distribution throughout the PVDF matrix. As shown in the figures, rGO exhibits a rough surface with a wrinkled structure, MWCNTs appear as hollow cylinders with lighter contrast, and AgNWs display a solid cylindrical structure with a darker contrast compared to MWCNTs.

Fig. 3(a) reveals the pressure-dependent resistance of the PVDF/NF-2, PVDF/NF-4, and PVDF/NF-6 pressure sensors. As shown, the resistance of the sensors decreases with applied pressure. The decrease is more pronounced for the PVDF/NF-2 sensor and less for the PVDF/NF-6 sensor across the entire applied pressure range from 0 to 300 kPa. This trend is attributed to the highly porous structure of PVDF/NF-2, while PVDF/NF-6 has a less porous structure, which is consistent with our previous work on foam-based pressure sensors.[10] The pressure-dependent resistance of a commercial pressure sensor (FlexiForce A401, Tekscan, USA) follows a similar trend of resistance decrease under applied pressure compared to the fabricated sensors, as shown in Fig. S4 of the ESI.†

Fig. 3(b) presents the relative change in resistance as a function of pressure for the FlexiForce A401, PVDF/NF-2, PVDF/NF-4, and PVDF/NF-6 sensors. The sensitivity (S) of each pressure sensor is measured as the slope of the relative change in resistance *versus* pressure graph, calculated using the following equation:

$$S = \frac{\delta\left(\frac{\Delta R}{R_0}\right)}{\delta p}$$

where ΔR is the change in resistance, R_0 is the resistance under zero pressure, p is the applied pressure, and the relative change in resistance ($\Delta R/R_0$) is determined as the percentage change (%). The sensitivity of the sensor was calculated using the above equation from Fig. 3(b) under low, medium, and high-pressure regimes. In the low, medium, and high-pressure regimes, PVDF/NF-2 exhibited sensitivities of 10.67, 0.43, and 0.014 kPa^{-1}; PVDF/NF-4 showed sensitivities of 10.26, 0.33, and 0.016 kPa^{-1}; and PVDF/NF-6 demonstrated sensitivities of 10.74, 0.30, and 0.029 kPa^{-1}, respectively. Fig. S5 and the inset of Fig. 3(a) show the schematic illustration that reveals the sensing mechanism of the PVDF/NF sensor. As shown in the figure, the contact area between the carbon-coated Al electrodes and the PVDF/NF active layer increases significantly, resulting in a decrease in contact resistance under the low-pressure regime. Simultaneously, there is a slight decrease in the interlayer gap and a reduction in porosity due to pore compression, leading to a significant decrease in the sensor's resistance under low pressure, thus exhibiting high sensitivity. As pressure increases in the medium and high-pressure regimes, the resistance of the sensor gradually decreases due to further reduction in the interlayer gap and porosity, resulting in lower sensitivity. Eventually, the sensor signal becomes almost saturated.

Low hysteresis is essential for sensors to ensure reliable reversible sensing performance. Fig. S6 in the ESI† illustrates the sensor's response during the loading and unloading cycles. As depicted, the sensor exhibited a hysteresis of 9.62%. Fig. 3(c) illustrates the relative change in resistance of the sensor under cyclic pressures of 55.6 kPa, 73.8 kPa, 97.8 kPa, 150.5 kPa, and 203.9 kPa when the sensor is pre-subjected to a pressure of 51.7 kPa. The sensor displays stable performance with a transient response during the loading and unloading phases, indicating its capability to function effectively across various pressures.

Fig. 3(d) presents the relative change in resistance as a function of time under stepwise loading and unloading, with pressure values ranging from 18.1 kPa to 115.2 kPa. The pressure is held for 5 seconds after each loading and unloading step to investigate the signal drift of the sensor. Drift refers to the variation in the sensor's response over time when exposed

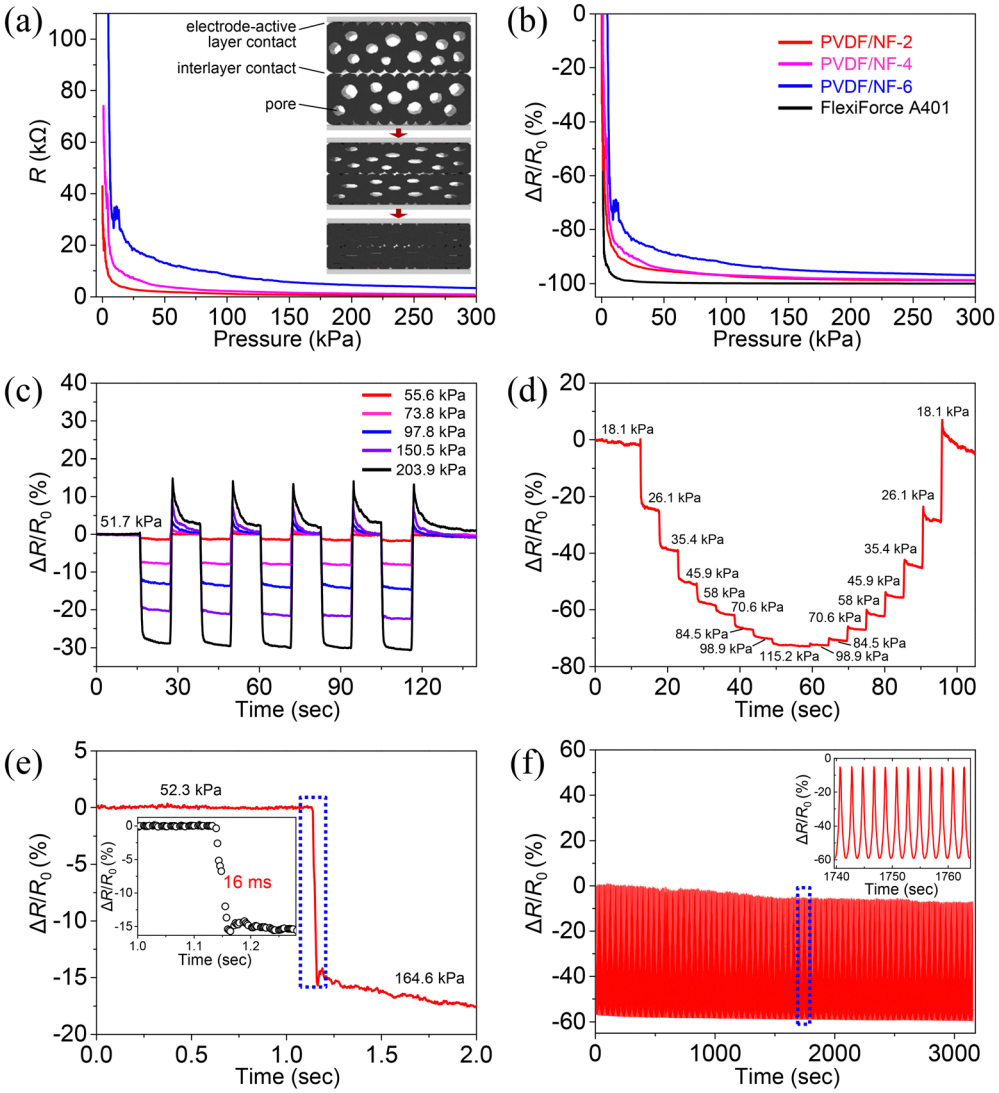

Fig. 3 Device electro-mechanical performance: (a) pressure-dependent resistance of PVDF/NF-2, PVDF/NF-4, and PVDF/NF-6, (b) pressure-dependent relative change in resistance for FlexiForce A401, PVDF/NF-2, PVDF/NF-4, and PVDF/NF-6, (c) sensor response under cyclic pressures of 55.6 kPa, 73.8 kPa, 97.8 kPa, 150.5 kPa, and 203.9 kPa, (d) drift response of the sensor during stepwise loading and unloading between 18.1 kPa and 115.2 kPa, (e) sensor response time (inset shows the relative change in resistance under applied pressure), and (f) cyclic stability and durability of the sensor under a cyclic pressure of 60 kPa.

to a constant pressure for an extended period.[45] As shown in the figure, the sensor exhibits a small drift under stepwise loading and unloading, which may be attributed to stress relaxation caused by the elastic–viscoplastic nature of the PVDF matrix.[46] The sensor response time is determined to be 16 ms following a sudden pressure increase from 52.3 kPa to 164.6 kPa, as shown in Fig. 3(e). The sensor's long-term behavior under 60 kPa cyclic pressure is shown in Fig. 3 (f), highlighting its stability and durability across 1500 cycles. The inset of Fig. 3(f) provides a zoomed-in view of the sensor's response to cyclic pressure. Table 1 shows a comparison of the performance parameters of the electrospinning-based pressure sensor and our sensor. As shown in the table, the PVDF/NF pressure sensor exhibited comparable performance in terms of sensitivity and pressure range. Moreover, our sensor demonstrated a faster response time than the reports listed in the table.[24,25,27–32]

As shown in Fig. 3(f), the cyclic stability and durability of the pressure sensor were tested under a cyclic pressure of 60 kPa at a frequency of 0.5 Hz. To investigate the sensor's response to higher-frequency periodic pressure, it was securely mounted on a mini-shaker, which applied consistent periodic pressure, allowing for precise tracking of resistance variations as shown in Fig. 4(a). The sensor was pre-exposed to random pressures to facilitate the effective transfer of periodic pressure. Fig. 4(b) reveals the relative change in resistance of the sensor under different cyclic pressures at frequencies of 1 Hz, 10 Hz, 50 Hz, 100 Hz, 200 Hz, 300 Hz, 400 Hz, and 500 Hz, respectively. As shown in Fig. 4(b), the sensor successfully detected and responded to pressure changes within the measured

Table 1 Comparison of performance parameters of the electrospinning-based pressure sensor and our sensor

Materials	Pressure range (kPa)	Sensitivity (kPa^{-1})	Response time (ms)	Cycles	Ref.
PVA/CNT coated PVDF fibrous network	40	0.0196	NA	350	25
PEDOT/MWCNT loaded PU mat	70	0.056–1.6	80	18 000	31
Ag coated PU nanofiber film	15	0.97–10.5	60	10 000	29
PAN/Al_2O_3 carbonization	4.5	0.025–1.41	300	5000	28
c-MWCNT decorated TPU fibrous network	10	0.02–2	70	1000	30
PVP@PPy/PAN nanofibers	2	11.5	170	1500	27
MXene coated TPU/PAN/F127 membrane	160	0.0078–0.208	60	8000	32
ILs/MWCNTs/PVDF	307	0.0002–0.075	180	1400	24
PVDF/MWCNT/rGO/AgNWs	300	0.014–10.67	16	1500	This work

frequencies, highlighting its suitability for real-time pressure monitoring across a wide frequency range. Fig. S7(a)–(f) (ESI†) show the enlarged views of the high-frequency pressure measurements at 50 Hz, 100 Hz, 200 Hz, 300 Hz, 400 Hz, and 500 Hz, respectively. In Fig. 4(c), the sensitivity obtained from Fig. 4(b) is shown as a function of the input frequency. The sensitivity peaks at 400 Hz then decreases as the frequency continues to increase. This demonstrates that the sensor is highly effective not only for static sensing but also for dynamic sensing within the frequency range of up to 500 Hz. Table S2 in the ESI† shows the dynamic pressure bandwidths of recently reported piezo-resistive pressure sensors in comparison with the PVDF/NF sensor.

Due to its good response to cyclic pressure in both lower and higher frequency regimes, the sensor can be utilized in various applications, including machine vibration sensing and human health monitoring. To demonstrate its potential application in machine vibration sensing, it has been firmly attached along with a commercial accelerometer (352A56, PCB Electronics) onto a vacuum pump (DOA-P704-AC, Gast Manufacturing, USA) using Scotch tape as shown in Fig. 5(a). This setup allows for the simultaneous measurement of acceleration and voltage variations associated with vibrations. Fig. 5(b) displays an optical image of a voltage divider circuit used to measure the voltage variation across the pressure sensor under vacuum pump vibrations.

The circuit features a PVDF/NF sensor as a variable resistor (R_s) connected in series with a 10 kΩ fixed resistor (R_f), powered by a 9 V DC voltage (V_i). Voltage variations across the sensor and the acceleration were simultaneously measured using the DAQ. The voltage variation across the sensor is calculated using the following expression:

$$V_s = \frac{R_s}{R_s + R_f} V_i$$

where V_s is the voltage across the sensor, R_s is the resistance of the sensor, R_f is the fixed resistance and V_i is the supply voltage. The equivalent voltage divider circuit diagram for vibration sensing, including both the sensor and the accelerometer, is provided in Fig. S8 of the ESI.† Fig. 5(c) and (d) show the time-domain acceleration signal from the accelerometer and the voltage signal from the pressure sensor, respectively, under vacuum pump operating conditions. These time-domain signals were further analyzed to obtain the frequency-domain spectrum *via* fast Fourier transformation (FFT) using MATLAB. Fig. 5(e) and (f) reveal the

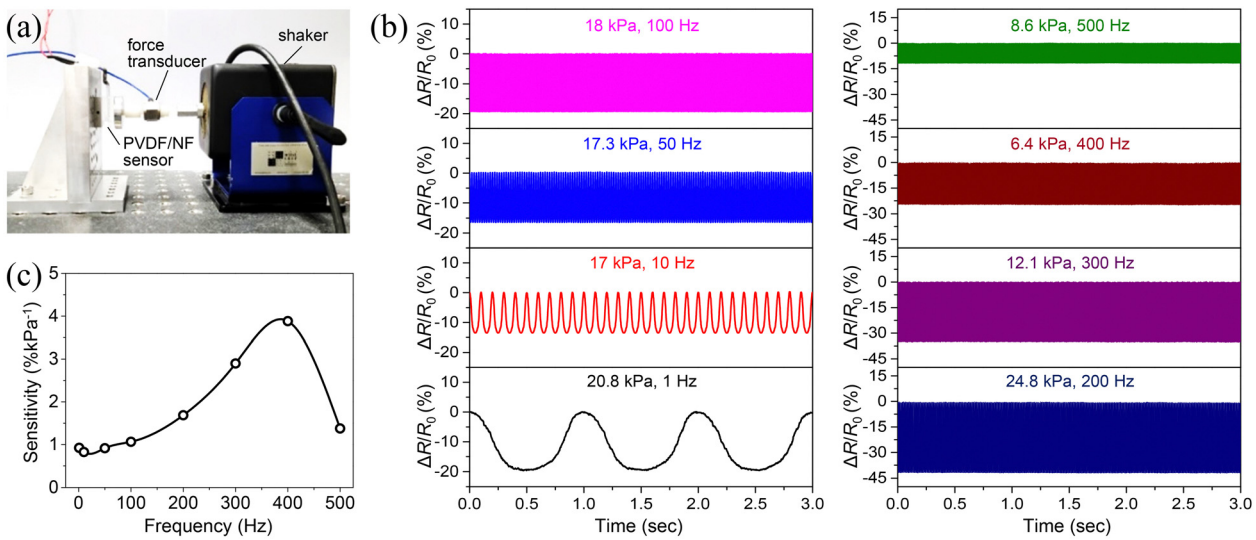

Fig. 4 Sensor response to cyclic pressure from shaker: (a) optical images showing the sensor mounted on a shaker, (b) relative change in resistance of the sensor under cyclic pressures at various frequencies: 20.8 kPa at 1 Hz, 17 kPa at 10 Hz, 17.3 kPa at 50 Hz, 18 kPa at 100 Hz, 24.8 kPa at 200 Hz, 12.1 kPa at 300 Hz, 6.4 kPa at 400 Hz, and 8.6 kPa at 500 Hz, and (c) sensitivity as a function of applied pressure frequency.

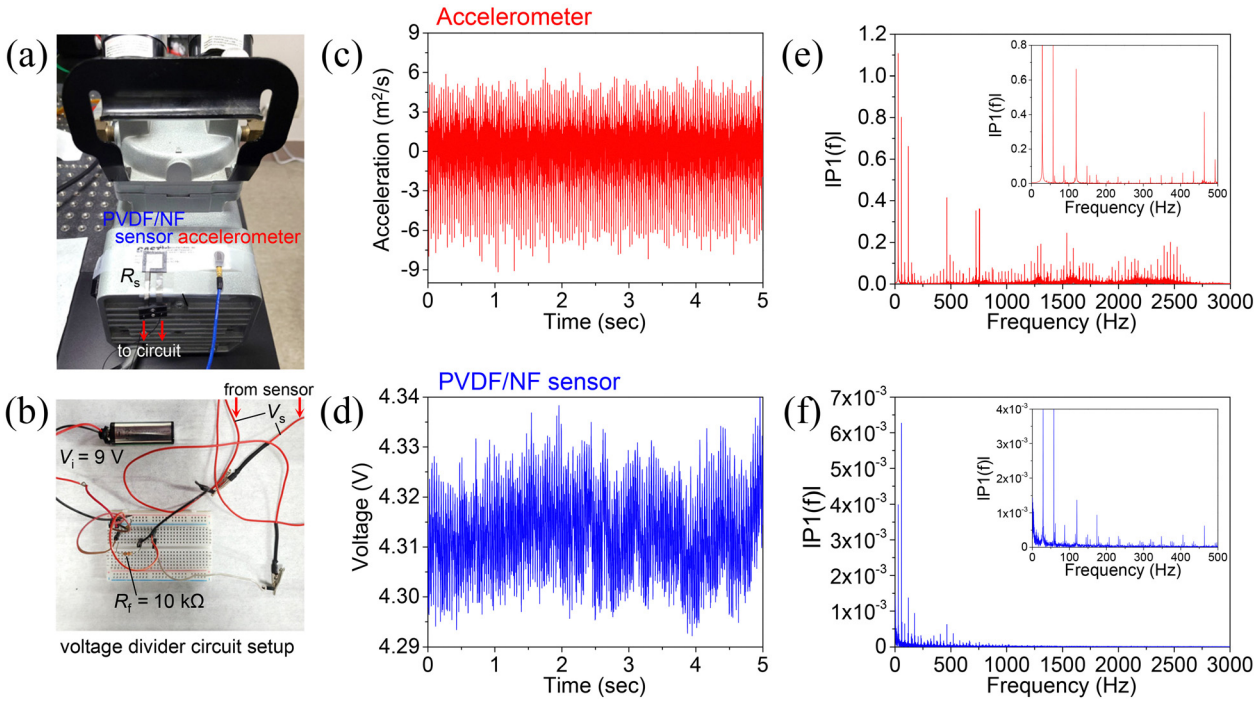

Fig. 5 Applications in vacuum pump vibration detection: (a) photo showing the sensor and accelerometer attached to a vacuum pump, (b) optical image of a voltage divider circuit used to measure voltage changes across the pressure sensor, (c) acceleration measured by the accelerometer during pump operation, (d) voltage variation of the pressure sensor during pump operation, and (e)–(f) frequency-dependent FFT spectra of the signals from the accelerometer and the sensor, with insets providing an enlarged view of the frequency spectrum.

vibration frequency spectrum of the vacuum pump, obtained from the accelerometer and the voltage response monitoring, respectively. The insets of Fig. 5(e) and (f) present an enlarged view of the spectrum in the range of 1–500 Hz of the accelerometer and the sensor, respectively. As shown in the inset of Fig. 5(e) and (f), frequency harmonics are observed in the spectrum. Such frequency harmonics are commonly associated with vibrations in rotating machinery. Specifically, the first peak at approximately 30 Hz is likely a 1/2-order subharmonic resonance, considering the rotor's rotation speed of around 60 Hz. These 1/2-order subharmonics are understood to result from the system's nonlinearity. They are reported to occur under specific conditions, such as when the system's equilibrium position shifts from the central axis, when internal clearance in ball bearings develops, or when cracks form in the rotor.[47–50] In addition, Fig. S9(a) and (b) in the ESI† present an enlarged view of the spectrum in the range of 500–1000 Hz. As shown in the figures, the sensors were able to detect all frequencies up to 1 kHz, although the amplitudes were lower compared to those measured by a commercial accelerometer.

The wearable applications of the pressure sensor are demonstrated by attaching it to various parts of the human body using Scotch tape and monitoring the sensor signals associated with different human motions, as shown in Fig. 6(a)–(f). Fig. 6(a) reveals the variation of the sensor signal to repeated pressing and releasing under light, medium, and heavy pressure by an index finger. As shown in the figure, the peak value of the relative change in resistance of the sensor decreases with increasing pressure by an index finger. In addition, the pressure sensor was able to detect index finger movements, such as bending and straightening, as shown in Fig. 6(b). Fig. 6(c) and (d) show the pressure sensor's response to the flexion and extension of the wrist and knee joints, respectively. As shown in the figures, pressure is exerted on the sensor under joint flexion conditions resulting in a decrease in the relative change resistance of the sensor and reaching the initial value upon joint extension. Fig. 6(e) displays the pressure sensor response to foot pressure under walking and jogging pace when a sensor is mounted on the floor, revealing that the sensor could recognize the walking and jogging. The sensor detects pressure fluctuations during wrist pulse measurement, responding to each heartbeat, which is calculated to be around 70, matching the typical heartbeat of a healthy adult, as shown in Fig. 6(f). As blood moves through the arteries, the sensor captures these pressure changes and converts them into a pulse signal with all significant features such as a forward wave, reflected wave, and a dicrotic notch, providing real-time health insights.

4. Conclusions

In this study, we developed a high-performance pressure sensor by fabricating it using PVDF/NF ink *via* NFES. The PVDF/NF ink is prepared by dispersing 1D–2D NF into the PVDF matrix. NFES has emerged as an advanced printing technology that allows for the creation of precise and controllable 2D and 3D

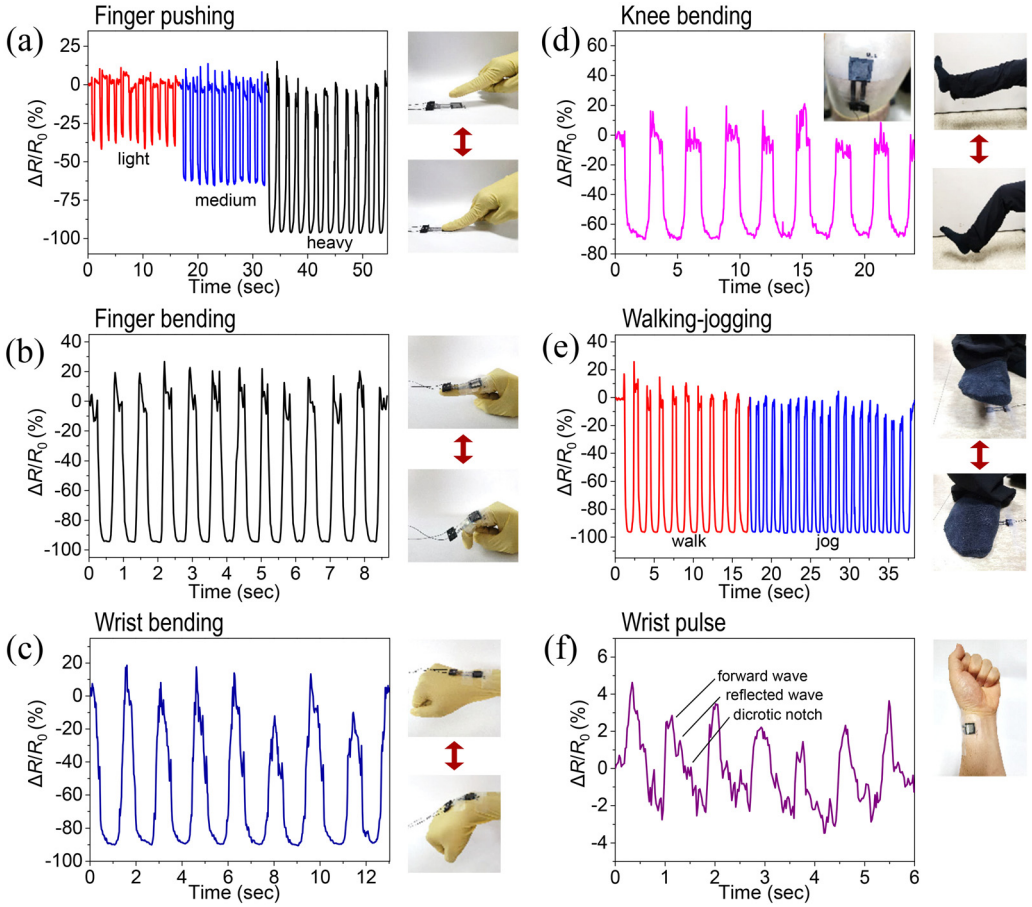

Fig. 6 Applications in human body movement detection: (a) relative change in resistance of the pressure sensors during repeated pressing and releasing with light, medium, and heavy pressure applied through an index finger, (b) response of the pressure sensor to the bending and straightening of the index finger, (c) and (d) response of the pressure sensor to wrist and knee flexion and extension, respectively, (e) relative change in resistance of the sensor mounted on the floor and subjected to pressure from the foot during walking and jogging, and (f) monitoring of wrist pulse signals using the pressure sensor.

structures with complex geometries. Sensors were fabricated with 2, 4, and 6 printing cycles, and their electromechanical performance was characterized. Each printing cycle follows a trajectory consisting of a cyclic rectangular path, 1 mm in width and 18 mm in length, with movements along both the *X*-axis and *Y*-axis directions.

The fabricated sensors demonstrate a broad pressure sensing range from 0 to 300 kPa and exhibit sensitivity values ranging from 0.014 to 10.67 kPa^{-1}. They also feature an exceptionally fast response time of 16 ms and a low hysteresis of 9.62%, enabling real-time pressure monitoring. In terms of durability, the sensors remain robust, withstanding over 1500 pressure cycles without significant degradation in performance. Furthermore, the sensor is capable of detecting pressure fluctuations at frequencies as high as 500 Hz, making it suitable for applications that require both low-frequency detection, such as monitoring human motion, and high-frequency detection, relevant for machine vibrations.

These results emphasize the PVDF/NF pressure sensor's broad potential, from wearable health devices to industrial machinery. Future research could focus on optimizing material compositions for NFES-based porous sensors to enhance key device parameters while developing efficient, multi-functional sensors for a wide range of real-world applications.

Author contributions

R. R. Kisannagar: writing original draft, review and editing, investigation, formal analysis, and data curation. J. Lee: conceptualization, methodology, and investigation. Y. Park: resources and methodology. I. Jung: supervision, funding acquisition, conceptualization, methodology, and review and editing.

Data availability

The data that support the findings of this study are available from the corresponding author upon reasonable request.

Conflicts of interest

The authors declare that they have no conflicts of interest.

Acknowledgements

This research was supported by the Brain Pool program funded by the Ministry of Science and ICT through the National Research Foundation of Korea (RS-2024-00405682) and the National Research Foundation of Korea (NRF) grant funded by the Korean government (MSIT) (RS-2023-NR076543).

References

1 J. T. Qu, G. M. Cui, Z. K. Li, S. T. Fang, X. R. Zhang, A. Liu, M. Y. Han, H. D. Liu, X. Q. Wang and X. H. Wang, *Adv. Funct. Mater.*, 2024, **34**, 2401311.
2 H. X. Yu, Q. Z. Wang, R. J. Xu, T. Sun, Q. H. Zhou, R. Dhakal, L. Chernogor, D. J. Zhang, Y. Y. Li, Y. Li and Z. Yao, *Chem. Eng. J.*, 2024, **490**, 151592.
3 S. Mishra, S. Mohanty and A. Ramadoss, *ACS Sens.*, 2022, **7**, 2495–2520.
4 X. R. Zhi, S. F. Ma, Y. F. Xia, B. Yang, S. Y. Zhang, K. T. Liu, M. Y. Li, S. H. Li, W. Peiyuan and X. Wang, *Nano Energy*, 2024, **125**, 109532.
5 Y. Zhang, X. M. Zhou, N. Zhang, J. Q. Zhu, N. N. Bai, X. Y. Hou, T. Sun, G. Li, L. Y. Zhao, Y. C. Chen, L. Wang and C. F. Guo, *Nat. Commun.*, 2024, **15**, 3048.
6 J. E. Hyun, T. Lim, S. H. Kim and J. H. Lee, *Chem. Eng. J.*, 2024, **484**, 149464.
7 M. Kim, I. Doh, E. Oh and Y. H. Cho, *ACS Appl. Nano Mater.*, 2023, **6**, 22025–22035.
8 D. Kwon, T. I. Lee, J. Shim, S. Ryu, M. S. Kim, S. Kim, T. S. Kim and I. Park, *ACS Appl. Mater. Interfaces*, 2016, **8**, 16922–16931.
9 Y. Q. Lei, J. H. Yang, Y. Xiong, S. S. Wu, W. D. Guo, G. S. Liu, Q. J. Sun and Z. L. Wang, *Chem. Eng. J.*, 2023, **462**, 142170.
10 J. Lee, J. Kim, Y. Shin and I. Jung, *Composites, Part B*, 2019, **177**, 107364.
11 R. K. Rajaboina, U. K. Khanapuram and A. Kulandaivel, *Adv. Sens. Res.*, 2024, **32**, 400045.
12 P. Supraja, R. R. Kumar, S. Mishra, D. Haranath, P. R. Sankar and K. Prakash, *Eng. Res. Express*, 2021, **3**, 035022.
13 C. S. Xu, J. Chen, Z. F. Zhu, M. R. Liu, R. H. Lan, X. H. Chen, W. Tang, Y. Zhang and H. Li, *Small*, 2024, **20**, 2306655.
14 J. Li, L. C. Fang, B. H. Sun, X. X. Li and S. H. Kang, *J. Electrochem. Soc.*, 2020, **167**, 037561.
15 Y. R. Li, D. W. Jiang, Y. L. An, W. S. Chen, Z. H. Huang and B. Jiang, *J. Mater. Chem. A*, 2024, **12**, 6826–6874.
16 Y. W. Wei, X. W. Shi, Z. Q. Yao, J. C. Zhi, L. X. Hu, R. Yan, C. Q. Shi, H. D. Yu and W. Huang, *npj Flexible Electron.*, 2023, **7**, 13.
17 Z. Wang, J. J. Ding and R. S. Guo, *ACS Appl. Mater. Interfaces*, 2023, **15**, 4789–4798.
18 Y. Huang, B. B. Liu, W. Y. Zhang, G. R. Qu, S. Y. Jin, X. B. Li, Z. X. Nie and H. Zhou, *npj Flexible Electron.*, 2022, **6**, 92.
19 Y. Huang, X. Y. You, Z. Q. Tang, K. Y. Tong, P. Guo and N. Zhao, *Small Methods*, 2021, **5**, 2000842.
20 Y. Wang, T. Yokota and T. Someya, *NPG Asia Mater.*, 2021, **13**, 22.
21 Y. Q. Huang, Y. F. Li, Y. Zhang, H. S. Yu and Z. C. Tan, *Mater. Today Adv.*, 2024, **21**, 100461.
22 X. X. He, J. Zheng, G. F. Yu, M. H. You, M. Yu, X. Ning and Y. Z. Long, *J. Phys. Chem. C*, 2017, 8663–8678.
23 L. A. Mercante, R. S. Andre, M. H. M. Facure, D. S. Correa and L. H. C. Mattoso, *Chem. Eng. J.*, 2023, **465**, 142847.
24 D. Zhang, R. K. Zhang, J. T. Sun, J. X. Zhang, Q. Y. Zhao, H. Y. He, H. J. Huang, L. Yang and Y. P. Xu, *Sens. Actuators, A*, 2024, **367**, 115037.
25 Q. Zhou, T. J. Chen, S. J. Cao, X. Xia, Y. Bi and X. L. Xiao, *Appl. Phys. A: Mater. Sci. Process.*, 2021, **127**, 667.
26 L. Simon, S. Livi, G. M. O. Barra and C. Merlini, *ACS Omega*, 2024, **9**, 46104–46116.
27 X. Z. Lin, Y. Bing, F. Li, H. X. Mei, S. Liu, T. Fei, H. R. Zhao and T. Zhang, *Adv. Mater. Technol.*, 2022, **7**, 2101312.
28 Z. Y. Han, Z. Q. Cheng, Y. Chen, B. Li, Z. W. Liang, H. F. Li, Y. J. Ma and X. Feng, *Nanoscale*, 2019, **11**, 5942–5950.
29 B. Xue, H. Y. Xie, J. X. Zhao, J. M. Zheng and C. Y. Xu, *Nanomaterials*, 2022, **12**, 723.
30 S. M. Li, R. Q. Li, O. G. González, T. J. Chen and X. L. Xiao, *Compos. Sci. Technol.*, 2021, **203**, 108617.
31 Y. Y. Luo, L. B. Zhao, G. X. Luo, L. X. Dong, Y. Xia, M. Li, Z. P. Li, K. F. Wang, R. Maeda and Z. D. Jiang, *Microsyst. Nanoeng.*, 2023, **9**, 113.
32 K. Q. Chang, M. H. Guo, L. Pu, J. C. Dong, L. Li, P. M. Ma, Y. P. Huang and T. X. Liu, *Chem. Eng. J.*, 2023, **451**, 138578.
33 Y. P. Zang, F. J. Zhang, C. A. Di and D. B. Zhu, *Mater. Horiz.*, 2015, **2**, 140–156.
34 X. J. Chen, X. T. Lin, D. Y. Mo, X. Q. Xia, M. F. Gong, H. S. Lian and Y. H. Luo, *RSC Adv.*, 2020, **10**, 26188–26196.
35 D. H. Sun, C. Chang, S. Li and L. W. Lin, *Nano Lett.*, 2006, **6**, 839–842.
36 X. M. Cai, T. P. Lei, D. H. Sun and L. W. Lin, *RSC Adv.*, 2017, **7**, 15382–15389.
37 P. Martins, A. C. Lopes and S. Lanceros-Mendez, *Prog. Polym. Sci.*, 2014, **39**, 683–706.
38 R. Y. Yang, Y. Y. Tan, T. Zhou, Y. H. Xu, S. H. Qin, D. H. Zhang and S. Liu, *Polym. Compos.*, 2024, **45**, 11044–11061.
39 R. R. Kisannagar, P. Jha, A. Navalkar, S. K. Maji and D. Gupta, *ACS Omega*, 2020, **5**, 10260–10265.
40 T. Boccaccio, A. Bottino, G. Capannelli and P. Piaggio, *J. Membr. Sci.*, 2002, **210**, 315–329.
41 A. C. Lopes, C. M. Costa, C. J. Tavares, I. C. Neves and S. Lanceros-Mendez, *J. Phys. Chem. C*, 2011, **115**, 18076–18082.
42 Y. Bormashenko, R. Pogreb, O. Stanevsky and E. Bormashenko, *Polym. Test.*, 2004, **23**, 791–796.
43 Y. A. Barnakov, O. Paul, A. Joaquim, A. Falconer, R. Mu, V. Y. Barnakov, D. Dikin, V. P. Petranovskii, A. Zavalin, A. Ueda and F. Williams, *Opt. Mater. Express*, 2018, **8**, 2579–2585.
44 D. Punetha, M. Kar and S. K. Pandey, *Sci. Rep.*, 2020, **10**, 2151.

45 Z. Y. Nie, J. W. Kwak, M. D. Han and J. A. Rogers, *Adv. Mater.*, 2024, **36**, 2205609.
46 A. Santimetaneedol, R. Tripuraneni, S. A. Chester and S. P. V. Nadimpalli, *J. Power Sources*, 2016, **332**, 118–128.
47 C. Q. Bai, H. Y. Zhang and Q. Y. Xu, *Int. J. Nonlin. Mech.*, 2013, **50**, 1–10.
48 A. Bovsunovsky and C. Surace, *Mech. Syst. Signal Process.*, 2015, **62–63**, 129–148.
49 Y. Ishida and F. Lu, presented in part at the Asia-Pacific Vibration Conference, Kyungju, Korea, November 9–13, 1997.
50 C.-K. Namkoong and S.-W. Lee, *Trans. Korean Soc. Mach. Tool Eng.*, 2001, **10**, 43–50.